Boundary-artifact-free phase retrieval with the transport of intensity equation II: applications to microlens characterization

Chao Zuo,[1,2,*] Qian Chen,[1] Hongru Li,[2,3] Weijuan Qu,[4] and Anand Asundi[2]

[1]*Jiangsu Key Laboratory of Spectral Imaging & Intelligent Sense, Nanjing University of Science and Technology, Nanjing, Jiangsu Province 210094, China*

[2]*Centre for Optical and Laser Engineering, School of Mechanical and Aerospace Engineering, Nanyang Technological University, Singapore 639798, Singapore*

[3]*Department of Opto-Electronics, Sichuan University, No.24 of South Yihuan Road Section, Chengdu 610064, China*

[4]*Centre for Applied Photonics and Laser Technology, Ngee Ann Polytechnic, 535 Clementi Road, 599489 Singapore*

[*]*surpasszuo@163.com*

Abstract: Boundary conditions play a crucial role in the solution of the transport of intensity equation (TIE). If not appropriately handled, they can create significant boundary artifacts across the reconstruction result. In a previous paper [Opt. Express **22**, 9220 (2014)], we presented a new boundary-artifact-free TIE phase retrieval method with use of discrete cosine transform (DCT). Here we report its experimental investigations with applications to the micro-optics characterization. The experimental setup is based on a tunable lens based *4f* system attached to a non-modified inverted bright-field microscope. We establish inhomogeneous Neumann boundary values by placing a rectangular aperture in the intermediate image plane of the microscope. Then the boundary values are applied to solve the TIE with our DCT-based TIE solver. Experimental results on microlenses highlight the importance of boundary conditions that often overlooked in simplified models, and confirm that our approach effectively avoid the boundary error even when objects are located at the image borders. It is further demonstrated that our technique is non-interferometric, accurate, fast, full-field, and flexible, rendering it a promising metrological tool for the micro-optics inspection.

OCIS codes: (100.5070) Phase retrieval; (100.3010) Image reconstruction techniques; (120.5050) Phase measurement.

References and links

1. E. Cuche, F. Bevilacqua, and C. Depeursinge, "Digital holography for quantitative phase-contrast imaging," Opt. Lett. **24**(5), 291–293 (1999).
2. B. Kemper and G. von Bally, "Digital holographic microscopy for live cell applications and technical inspection," Appl. Opt. **47**(4), A52–A61 (2008).
3. J. R. Fienup, "Phase retrieval algorithms: a comparison," Appl. Opt. **21**(15), 2758–2769 (1982).
4. L. J. Allen and M. P. Oxley, "Phase retrieval from series of images obtained by defocus variation," Opt. Commun. **199**(1-4), 65–75 (2001).
5. M. Reed Teague, "Deterministic phase retrieval: a Green's function solution," J. Opt. Soc. Am. **73**(11), 1434–1441 (1983).
6. T. Gureyev, A. Roberts, and K. Nugent, "Phase retrieval with the transport-of-intensity equation: matrix solution with use of Zernike polynomials," JOSA A **12**(9), 1932–1942 (1995).
7. T. E. Gureyev and K. A. Nugent, "Phase retrieval with the transport-of-intensity equation. II. Orthogonal series solution for nonuniform illumination," J. Opt. Soc. Am. A **13**(8), 1670–1682 (1996).
8. V. V. Volkov, Y. Zhu, and M. De Graef, "A new symmetrized solution for phase retrieval using the transport of intensity equation," Micron **33**(5), 411–416 (2002).
9. C. Zuo, Q. Chen, Y. Yu, and A. Asundi, "Transport-of-intensity phase imaging using Savitzky-Golay differentiation filter--theory and applications," Opt. Express **21**(5), 5346–5362 (2013).

#210176 - $15.00 USD Received 14 Apr 2014; revised 9 Jun 2014; accepted 26 Jun 2014; published 22 Jul 2014

10. T. E. Gureyev, A. Roberts, and K. A. Nugent, "Partially coherent fields, the transport-of-intensity equation, and phase uniqueness," J. Opt. Soc. Am. A **12**(9), 1942–1946 (1995).
11. J. Martinez-Carranza, K. Falaggis, T. Kozacki, and M. Kujawinska, "Effect of imposed boundary conditions on the accuracy of transport of intensity equation based solvers," *Proc. SPIE,* 87890N (2013).
12. T. E. Gureyev and K. A. Nugent, "Rapid quantitative phase imaging using the transport of intensity equation," Opt. Commun. **133**(1-6), 339–346 (1997).
13. D. Paganin and K. A. Nugent, "Noninterferometric phase imaging with partially coherent light," Phys. Rev. Lett. **80**(12), 2586–2589 (1998).
14. J. Frank, S. Altmeyer, and G. Wernicke, "Non-interferometric, non-iterative phase retrieval by Green's functions," J. Opt. Soc. Am. A **27**(10), 2244–2251 (2010).
15. C. Zuo, Q. Chen, and A. Asundi, "Boundary-artifact-free phase retrieval with the transport of intensity equation: fast solution with use of discrete cosine transform," Opt. Express **22**(8), 9220–9244 (2014).
16. F. Charrière, J. Kühn, T. Colomb, F. Montfort, E. Cuche, Y. Emery, K. Weible, P. Marquet, and C. Depeursinge, "Characterization of microlenses by digital holographic microscopy," Appl. Opt. **45**(5), 829–835 (2006).
17. Q. Weijuan, C. O. Choo, Y. Yingjie, and A. Asundi, "Microlens characterization by digital holographic microscopy with physical spherical phase compensation," Appl. Opt. **49**(33), 6448–6454 (2010).
18. D. A. Gilbarg and N. S. Trudinger, *Elliptic Partial Differential Equations of Second Order* (Springer, 2001), Vol. 224.
19. I. W. Han, "New method for estimating wavefront from curvature signal by curve fitting," Opt. Eng. **34**(4), 1232–1237 (1995).
20. C. Zuo, Q. Chen, W. Qu, and A. Asundi, "High-speed transport-of-intensity phase microscopy with an electrically tunable lens," Opt. Express **21**(20), 24060–24075 (2013).
21. C. J. R. Sheppard, "Defocused transfer function for a partially coherent microscope and application to phase retrieval," J. Opt. Soc. Am. A **21**(5), 828–831 (2004).
22. C. Zuo, Q. Chen, W. Qu, and A. Asundi, "Noninterferometric single-shot quantitative phase microscopy," Opt. Lett. **38**(18), 3538–3541 (2013).
23. J. Martinez-Carranza, K. Falaggis, and T. Kozacki, "Optimum measurement criteria for the axial derivative intensity used in transport of intensity-equation-based solvers," Opt. Lett. **39**(2), 182–185 (2014).
24. L. Waller, L. Tian, and G. Barbastathis, "Transport of Intensity phase-amplitude imaging with higher order intensity derivatives," Opt. Express **18**(12), 12552–12561 (2010).
25. F. Morse, *Methods of Theoretical Physics* (2-Volume set) (McGraw-Hill, 1981).
26. P. Ferraro, S. De Nicola, A. Finizio, G. Coppola, S. Grilli, C. Magro, and G. Pierattini, "Compensation of the Inherent Wave Front Curvature in Digital Holographic Coherent Microscopy for Quantitative Phase-Contrast Imaging," Appl. Opt. **42**(11), 1938–1946 (2003).
27. T. Colomb, F. Montfort, J. Kühn, N. Aspert, E. Cuche, A. Marian, F. Charrière, S. Bourquin, P. Marquet, and C. Depeursinge, "Numerical parametric lens for shifting, magnification, and complete aberration compensation in digital holographic microscopy," J. Opt. Soc. Am. A **23**(12), 3177–3190 (2006).
28. C. Zuo, Q. Chen, W. Qu, and A. Asundi, "Phase aberration compensation in digital holographic microscopy based on principal component analysis," Opt. Lett. **38**(10), 1724–1726 (2013).
29. C. Zuo, Q. Chen, and A. Asundi, "Comparison of Digital Holography and Transport of Intensity for Quantitative Phase Contrast Imaging," in *Fringe 2013*, W. Osten, ed. (Springer Berlin Heidelberg, 2014), pp. 137–142.
30. D. Paganin, A. Barty, P. J. McMahon, and K. A. Nugent, "Quantitative phase-amplitude microscopy. III. The effects of noise," J. Microsc. **214**(1), 51–61 (2004).
31. N. Streibl, "Three-dimensional imaging by a microscope," J. Opt. Soc. Am. A **2**(2), 121–127 (1985).
32. E. D. Barone-Nugent, A. Barty, and K. A. Nugent, "Quantitative phase-amplitude microscopy I: optical microscopy," J. Microsc. **206**(3), 194–203 (2002).
33. C. Campbell, "Wave-front sensing by use of a Green's function solution to the intensity transport equation: comment," J. Opt. Soc. Am. A **24**(8), 2480–2481, discussion 2482–2484 (2007).
34. S. C. Woods, H. I. Campbell, and A. H. Greenaway, "Wave-front sensing by use of a Green's function solution to the intensity transport equation: reply to comment," J. Opt. Soc. Am. A **24**(8), 2482–2484 (2007).
35. T. Gureyev and S. Wilkins, "On X-ray phase retrieval from polychromatic images," Opt. Commun. **147**(4-6), 229–232 (1998).

1. Introduction

Amplitude and phase are two key components for a complete description of an optical wave. When a wavefield interacts with an object, not only the incident amplitude distribution is modulated by the absorption but the incoming phase distribution is modified by the phase of the object. For many specimens, such as optical components and biological samples, the effects of phase are more important than the effects of absorption because they affect the phase with only minimal effect on the intensity. However, though the intensity of the wavefield is relatively easy to measure, the phase is not accessible directly. Therefore, optical phase retrieval becomes a central problem throughout physics and optics. Several techniques

#210176 - $15.00 USD Received 14 Apr 2014; revised 9 Jun 2014; accepted 26 Jun 2014; published 22 Jul 2014

exist to determine the phase distribution of the wavefield, which can be classified into two main categories, namely interferometric techniques, for instance, holographic methods [1, 2], and non-interferometric techniques (so-called phase retrieval). Non-interferometric techniques can be further divided into two subsets: iterative methods [3, 4], and deterministic methods [5–9]. Due to its simple experimental arrangement and low requirement for the illumination coherence, this work focuses on the deterministic phase retrieval technique based on the transport of intensity equation (TIE) [5]. This equation describes the relationship between the derivative of intensity in the light propagation direction and the phase of a light wave in near Fresnel regime. Assuming a paraxial beam described by $\sqrt{I(\boldsymbol{r})}\exp[i\phi(\boldsymbol{r})]$, propagating along the z axis, the TIE states that

$$-k\frac{\partial I(\boldsymbol{r})}{\partial z}=\nabla\cdot\left[I(\boldsymbol{r})\nabla\phi(\boldsymbol{r})\right], \tag{1}$$

where k is the wave number $2\pi/\lambda$, $\boldsymbol{r}$ is the position vector representing the spatial coordinates (x,y), $I(\boldsymbol{r})$ is the intensity, located without loss of generality at the plane $z=0$, $\phi(\boldsymbol{r})$ is the phase to be retrieved. The axial intensity derivative $\partial I/\partial z$ can be experimentally obtained by finite differences with a minimum of two defocused intensity images taken at distinct planes separated by a small distance orthogonal to the optical axis. Suppose $I>0$ and with appropriate boundary conditions, the solution to the TIE is known to exist and be unique [10], i.e., the phase ϕ can be uniquely determined by solving the TIE with the determined intensity I and the axial intensity derivative $\partial I/\partial z$, in a non-iterative manner.

Despite its mathematical well-posedness, the rigorous implementation of the TIE phase retrieval tends to be difficult because the corresponding boundary conditions are not easy to obtain in practice. Such boundary conditions are usually based on *a priori* knowledge [11], for example, if the sample is isolatedly placed in the center of the camera field of view (FOV), surrounded by a unperturbed plane wave, then one can safely define some simplified boundary conditions, e.g., the homogeneous Dirichlet/Neumann boundary conditions, or the periodic boundary conditions. In this case, the most popular fast Fourier transform (FFT) based TIE solver [7, 12, 13] works well because it implies periodic boundary conditions due to the cyclic nature of the discrete Fourier transform. However, this situation is rather restrictive and does not reflect general experimental conditions. When the actual experimental situation violates those imposed assumptions, e.g., objects are located at the image borders, severe boundary artifacts will appear, seriously affecting the accuracy of the phase reconstruction [8, 11, 14]. To our knowledge, the boundary error problem is one major obstacle for the TIE to gaining extensive applications in the field of high-precision phase measurement.

To this end, we recently developed a new method to solve the TIE with experimentally measurable boundary conditions, though an efficient numerical algorithm with use of fast discrete cosine transform (DCT) [15]. The new method has several substantial advantages: First, it clearly defines the TIE phase retrieval as an ***inhomogeneous Neumann boundary*** value problem, and the corresponding boundary values can be directly measured around a hard-edged aperture located in the in-focus plane. Second, it is based on an elegant formulation that requires no *a priori* knowledge about the test object and special-purpose detection scheme to explicitly extract the boundary signals. Finally, it retains the major advantages of the FFT-based solvers – fast and computationally simple for the rectangular domain. Though the correctness and validity of the new method have been demonstrated by simulations in our previous paper [15], its practical performance is still a major concern. Therefore in this manuscript, we further present the experimental verification of this method, focusing on the specific applications of the micro-optics characterization. The main motivation to select micro-optical components as test objects is two-fold. On the one hand, micro-optical components, such as microlens arrays are typically composed of several lenses that form either an one-dimensional or two-dimensional array on a supporting substrate. For microlens arrays with high fill-factor, each individual lenslet inside the array is not isolated so

#210176 - $15.00 USD Received 14 Apr 2014; revised 9 Jun 2014; accepted 26 Jun 2014; published 22 Jul 2014

that it is quite difficult to arrange it to meet the above simplified (homogeneous/periodic) boundary conditions. Therefore, they are ideal examples to highlight the importance of boundary conditions in the solution of the TIE. On the other hand, the geometrical characteristics of micro-optical components determine their optical performance and imaging quality directly. Precise characterization of the shape, surface quality, and optical performance of the micro-optics are also extremely demanding, and of great significance in the quality evaluation and fabrication guidance. Though many different metrology approaches, such as contact profiler, confocal microscopy, interferometry are applicable for the shape measurement of the micro-optics [16, 17], here we first demonstrate the use of the TIE as a new non-contact, non-interferometric, accurate, fast, full-field, and flexible metrological tool for the micro-optics characterization.

2. The importance of boundary conditions in the solution of the TIE

An important issue in the phase retrieval problem is the uniqueness of the solution. Mathematically, the TIE is an elliptic partial differential equation for the phase function ϕ, and boundary conditions are required to solve the equation uniquely [18]. Therefore, the transport of intensity phase retrieval is essentially a boundary value problem (boundary value problem = partial differential equation + boundary conditions): seeking a solution to the TIE that also satisfies the given boundary conditions. We assume the region governed by the TIE to be a general open and bounded domain $\Omega \subset \mathbb{R}^2$ with a piecewise smooth boundary $\partial\Omega$. The intensity distribution I is a continuous, non-negative function defined on the enclosure $\bar{\Omega}$, and is smooth and strictly positive in Ω. The axial intensity derivative $\partial I/\partial z$ is assumed to be a smooth function in Ω. The phase ϕ is expected to be single-valued and smooth in $\bar{\Omega}$. In the following, we briefly introduce several classes of possible boundary conditions that could be applied to the solution of TIE:

(1) *Dirichlet boundary conditions.* The values of phase function ϕ are specified on the domain boundary

$$\phi|_{\partial\Omega} = g. \tag{2}$$

Here g is a smooth function on the boundary $\partial\Omega$.

(2) *Neumann boundary conditions.* The product of I and the normal derivative of ϕ, are specified on the domain boundary

$$I \frac{\partial \phi}{\partial n}\bigg|_{\partial\Omega} = g. \tag{3}$$

Here g is a smooth function on the boundary $\partial\Omega$, $\partial\phi/\partial n$ is the outward normal derivative.

(3) *Periodic boundary conditions*. The phase at the boundary repeats cyclically, e.g. for a rectangular domain, the phase at the right boundary is same as the phase at the left boundary.

With the determined intensity I, the axial intensity derivative $\partial I/\partial z$, coupled with one class of boundary conditions specified on $\partial\Omega$, the phase can be uniquely determined by solving the corresponding boundary value problem. Note the Dirichlet boundary value problem (Eq. (1) plus Eq. (2)) has a unique solution for phase [18], while solutions to Neumann (Eq. (1) plus Eq. (3)) and periodic boundary value problem are unique up to an unimportant additive constant [10, 15]. However, one important practical problem is that the corresponding boundary conditions are difficult to measure or to know *a priori* in practice (because the function g requires to know the phase value or phase normal derivative at the region boundary, which is quite hard since phase is what we want to measure), which poses severe difficulty to various TIE solvers.

The most well-known fast TIE solver is proposed by Paganin and Nugent [13], which involves the use of FFT to implement the inverse Laplacian operator. Despite its popularity, it implies periodic boundary conditions, forcing the phase outside the domain to be periodically

#210176 - $15.00 USD Received 14 Apr 2014; revised 9 Jun 2014; accepted 26 Jun 2014; published 22 Jul 2014

extended. When the opposite boundaries of the true phase distribution match poorly, this periodic assumption can cause serious boundary error across the reconstructed phase [11, 15]. It can be expected since generally the phase at the right boundary has nothing to do with the phase at the left boundary. Alternatively, Volkov *et al.* [8] suggest to symmetrically extend the intensity images into a four times larger size before using Paganin and Nugent's FFT-based solver to remedy the boundary error problem. This method has proven to work well in certain circumstances. Actually, taking the data outside the domain as a reflection of the data inside is equivalent to imposing two special cases of the (homogeneous) Dirichlet and the Neumann boundary conditions [11]:

(4) *Zero Dirichlet boundary* conditions (for odd symmetrization)

$$\phi\big|_{\partial\Omega} = 0. \tag{4}$$

(5) *Zero Neumann boundary* conditions (for even symmetrization)

$$I\frac{\partial\phi}{\partial n}\bigg|_{\partial\Omega} = 0. \tag{5}$$

In spite of the value of this technique, it does not guarantee the elimination of the boundary artifacts. It can still create significant boundary artifacts since the assumed boundary conditions may not coincide with the ground truth data. Figure 1 shows an example of boundary artifacts arising from a simulated complex object extending across the image boundary, reconstructed using the Paganin and Nugent's standard FFT-based method (Fig. 1(d)), the even symmetric extension method (Fig. 1(e)), and the odd symmetric extension method (Fig. 1(f)). Note severe boundary errors can be obviously observed in all results because of the fact that none of the three classes of boundary conditions ((3)-(5)) can be fulfilled completely. Such kind of artifacts does not just appear at image borders but propagates inside the domain and degrades the reconstruction accuracy prevailingly.

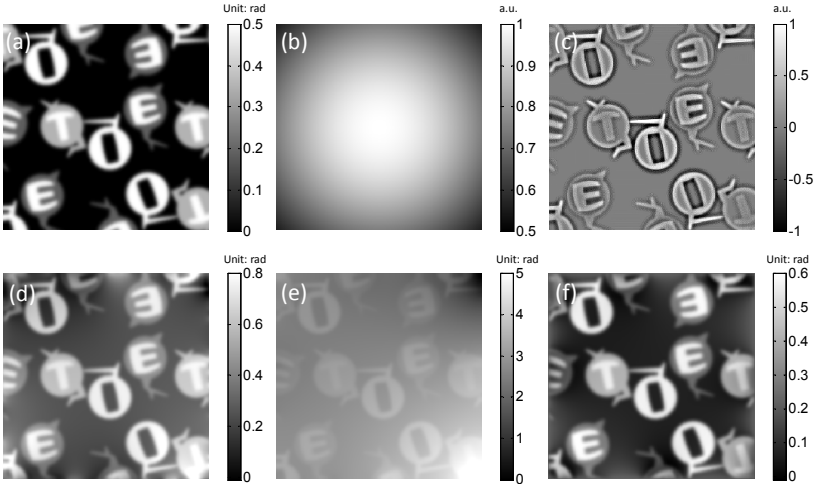

Fig. 1. Phase retrieval for a complex object covering the image boundary. (a) Phase distribution. (b) Intensity distribution. (c) Axial intensity derivative. (d) Phase retrieved by the FFT-based method (periodic boundary conditions). (e) Phase retrieved by the even symmetrization method (Zero Dirichlet boundary conditions). (f) Phase retrieved by the odd symmetrization method (Zero Neumann boundary conditions).

A common way to avoid this problem is to place the isolated sample in the center of the camera FOV, surrounded by an unperturbed plane wave, as shown in Fig. 2. In this way, the constant phase (corresponds to (4) zero Dirichlet boundary conditions), or zero phase change (corresponds to (5) zero Neumann boundary conditions), or even cyclically phase repetition

#210176 - $15.00 USD Received 14 Apr 2014; revised 9 Jun 2014; accepted 26 Jun 2014; published 22 Jul 2014

(corresponds to (3) periodic boundary conditions) at the image boundary can be satisfied. In such case, all these three methods can retrieve the phase accurately regardless of the selected boundary conditions. However, this configuration does not reflect general experimental conditions, and is impractical when the object is larger than the camera FOV. On the other hand, as illustrated in Fig. 1, when the actual experimental situation violates those imposed assumptions, significant boundary artifacts will appear in the final result. This kind of boundary error can obviously be a real problem when dealing with a complex object that must cover the image border, such as microlens arrays. Microlens arrays contain multiple lenses formed in a compact two-dimensional (hexagonal or square) array on a supporting substrate. If one wants to characterize one or some of individual lenses inside the array, it is not easy or even impossible to arrange the sample to meet the above simplified boundary conditions (3)-(5).

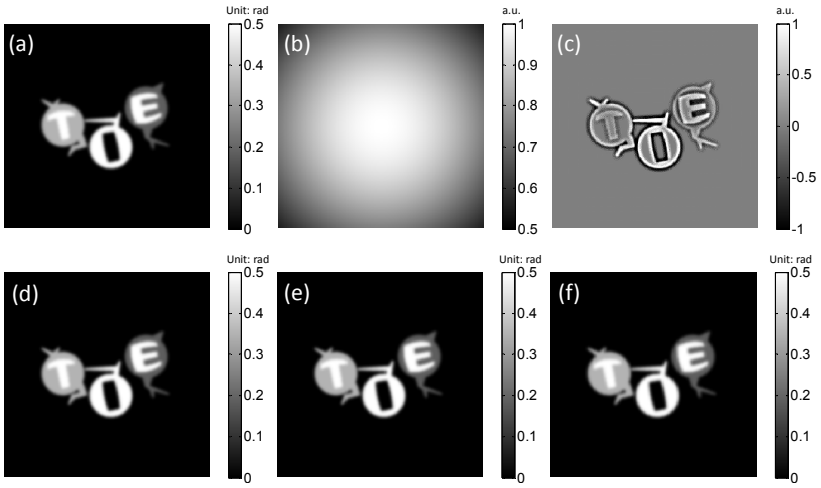

Fig. 2. Phase retrieval for an isolated object located in the central position. (a) Phase distribution. (b) Intensity distribution. (c) Axial intensity derivative. (d) Phase retrieved by the FFT-based method (periodic boundary conditions). (e) Phase retrieved by the even symmetrization method (Zero Dirichlet boundary conditions). (f) Phase retrieved by the odd symmetrization method (Zero Neumann boundary conditions).

3. Boundary-artifact-free phase retrieval with use of discrete cosine transform

As explained before, boundary artifacts mainly occur because the imposed boundary conditions do not coincide with the ground truth data. For complex objects like the one shown in Fig. 1, the precise knowledge of the (inhomogeneous) boundary conditions ((1)-(2), and $g \neq$ constant) is indispensable. Recently, we presented a theoretical investigation of a new DCT-based TIE solver as well as a new approach to get the associated boundary conditions [15]. The first step of the approach is to introduce a hard-edged aperture in the object plane (or its conjugated plane). Then the in-focus intensity image captured by the camera can be obviously represented as

$$I = A_\Omega I_0 = \begin{cases} I_0 & \mathbf{r} \in \bar{\Omega} \\ 0 & others \end{cases}, \tag{6}$$

where I_0 is the intensity when there is no aperture; A_Ω is the aperture function (A_Ω = 1 when $\mathbf{r} \in \bar{\Omega}$, A_Ω = 0 when $\mathbf{r} \notin \bar{\Omega}$). The function of the aperture is to generate the required inhomogeneous Neumann boundary conditions (Eq. (3)) for solving the TIE. Substituting Eq. (6) into the TIE (Eq. (1)), it can be derived that for this particular intensity distribution, the intensity transport can be written in the following form [15]

#210176 - $15.00 USD Received 14 Apr 2014; revised 9 Jun 2014; accepted 26 Jun 2014; published 22 Jul 2014

$$-k\frac{\partial I}{\partial z}=A_{\Omega}\left(I_0\nabla^2\phi+\nabla I_0\cdot\nabla\phi\right)-I\frac{\partial\phi}{\partial n}\delta_{\partial\Omega}. \tag{7}$$

where $\delta_{\partial\Omega}$ is the Dirac delta function around the aperture edge. Equation (7) suggests that the axial intensity derivative signals (longitudinal variations of the intensity) consist of two non-overlapping components: (1) the intensity variation inside the domain due to the phase slope and curvature as if the aperture is not present; (2) a delta-function-like signal sharply peaked at the aperture boundary, which provides the exact Neumann boundary conditions for the TIE (Eq. (3)). Since the whole axial intensity derivative (the LHS of Eq. (7)) is experimentally measurable through finite difference scheme (note the aperture must be smaller than the image FOV so that all the boundary signals can be captured), and the two RHS terms do not overlap in space, there is enough information to solve the TIE uniquely without requiring *a prior* knowledge of the boundary conditions. The inhomogeneous boundary value problem has been proven to be ***well-posed***, because it automatically satisfies the following compatibility condition (derived from integrating both sides of Eq. (7) over all space) [15]:

$$\iint_{\bar{\Omega}}-k\frac{\partial I(\mathbf{r})}{\partial z}\mathrm{d}\mathbf{r}=\iint_{\Omega}-k\frac{\partial I(\mathbf{r})}{\partial z}d\mathbf{r}-\oint_{\partial\Omega}I(\mathbf{r})\frac{\partial\phi(\mathbf{r})}{\partial n}\mathrm{d}s=0, \tag{8}$$

The physical picture described by Eq. (8) is just the ***energy conservation law*** – the total energy (intensity) of an isolated region is constant and unchangeable, and the loss of energy inside the region arising from energy flow across the region boundary.

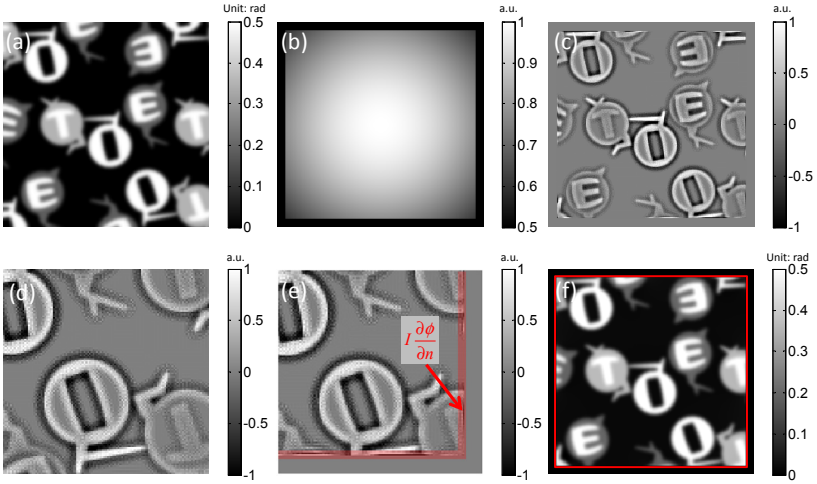

Fig. 3. Phase retrieval for a complex object covering the image boundary with the DCT-based method. (a) Phase distribution. (b) Intensity distribution (with a square aperture). (c) Axial intensity derivative. (d) Enlarged region corresponding to the lower right quarter of Fig. 1(c). (e) Enlarged region corresponding to the lower right quarter of Fig. 3(c), boundary signals can be clearly observed along the aperture edge (red shaded areas). (f) Phase retrieved by the DCT-based method (inhomogeneous Neumann boundary conditions). The red box in (f) outlines the aperture edge.

A detailed derivation of the DCT-based solver can be found in [15], and the final solution of the phase takes the following form

$$\phi(\mathbf{r})=-k\nabla_{DCT}^{-2}\nabla_{DCT}\left[I^{-1}(\mathbf{r})\nabla_{DCT}\nabla_{DCT}^{-2}\frac{\partial I(\mathbf{r})}{\partial z}\right], \tag{9}$$

where ∇_{DCT} and ∇_{DCT}^{-2} are respectively the gradient and inverse Laplacian operator calculated through DCT-based approaches (see Appendix C of [15] for details). It should be noted that

#210176 - $15.00 USD Received 14 Apr 2014; revised 9 Jun 2014; accepted 26 Jun 2014; published 22 Jul 2014

all the source data and related computations must be strictly limited to the rectangular-shaped area $\bar{\Omega}$, which includes both the aperture boundary and the region inside it (so that all the boundary signals can be enclosed in $\bar{\Omega}$). In this way, the measured intensity derivative can be treated as one entity, without requiring special-purpose detection scheme to explicitly extract the boundary signals (which has been known to cause serious difficulties [6, 19]).

Figure 3 shows the same sample as in Fig. 1 but reconstructed through the proposed approach. A rectangular aperture is introduced in the in-focus plane (Fig. 3(b)) and the corresponding axial intensity derivative is shown in Fig. 3(c). From the enlarged regions shown in Figs. 3(d) and 3(e), it can be clearly seen that the aperture generates additional boundary signals (corresponds to the second term on the RHS of Eq. (3)) which cannot be observed in the absence of the aperture. With correct boundary conditions as well as the corresponding DCT-based TIE solver, the reconstructed result is free from any boundary artifacts, and closely matches the ground-truth image (Fig. 3(f)).

In our previous paper and the above example, the DCT-based TIE solver is only supported only with nice computer simulations in the absence of experiments. Its actual performance under trivial practical issues like image noise, optical misalignment, and imperfection of sharp aperture is still unclear. Therefore, in the remaining of this paper, we will present some experimental results to demonstrate its practical capabilities with applications to the micro-optics characterization.

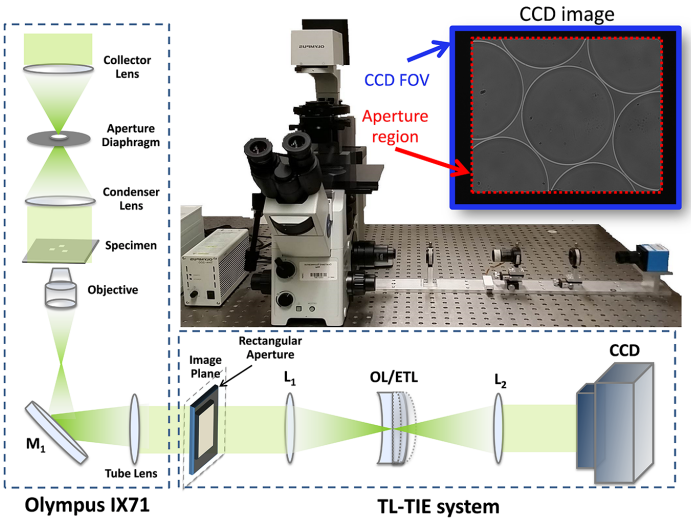

Fig. 4. Experimental configuration. A 4*f* system with OL/ETL located at the Fourier plane is attached to Olympus IX71 bright field microscope. The Fourier lens L_1 relays the back focal plane of the objective onto the OL/ETL. Fourier lens L_2 reconstructs the final image at the CCD plane, which is conjugated with the intermediate image plane. A rectangular aperture is placed in the intermediate image plane (conjugated object plane) of the microscope to fit the camera sensor area. The focal lengths of the lens L_1 and L_2 are both 150mm. The tunable focal length range of the ETL is from + 50 to + 200 mm. The change of the focus positions can be realized by adjusting the focal length of the ETL.

4. Experiments

The experimental configuration used for the present study is based on a tunable lens based TIE (TL-TIE) system, described in detail in [20]. As illustrated in Fig. 4, the whole setup is built upon a commercial inverted bright-field microscope (Olympus IX71), with the TL-TIE system as an add-on module attached to the camera port of the microscope. The illumination from the built-in halogen lamp was filtered by the green interference filter with a central wavelength of 550 nm and a pass-band of 45 nm. The microscope, composed of a collector lens, condenser aperture diaphragm, condenser lens, objective, reflective mirror (M_1), and

#210176 - $15.00 USD Received 14 Apr 2014; revised 9 Jun 2014; accepted 26 Jun 2014; published 22 Jul 2014

tube lens, produces a magnified image of the specimen at the intermediate image plane (camera port). Throughout our experiments, the samples were imaged with a bright-field 10 × objective (NA_{obj} = 0.25) and the condenser aperture was closed to the minimum value (NA_{cond} = 0.09) to optimize the illumination coherence (the coherent parameter S = NA_{cond}/NA_{obj} = 0.36) [21, 22]. The TL-TIE module comprises a standard 4f system with an electrically tunable lens (EL-C-10-30-VIS-LD, Optotune AG, Switzerland) combined with a plane concave offset lens (OL, focal length 100 mm) located at its Fourier plane. The images are captured by a monochrome CCD camera (The Imaging Source DMK 41AU02, 1280 × 960, 4.65μm pixel size, 15 fps). The premise behind this configuration is to avoid the mechanical adjustment of the setup during image capture. It should be noted that the basic theory and results presented herein are not just limited to this specific configuration, but also applicable to other conventional TIE imaging setups.

Note the key difference between the current configuration and the one reported in [20]: an additional rectangular aperture was introduced in the intermediate image plane of the microscope to generate the required boundary conditions for solving the TIE. The aperture was punched on a small sheet of stiff paper using a laser marking system. A variety of micro-optical components were studied and some of these are given below as representatives of the set. Without loss of the generality, the specimens were randomly placed so that neither the Zero Dirichlet/Neumann boundary conditions nor the periodic boundary conditions can be satisfied. In the experiments, the intensity derivative $\partial I/\partial z$ was estimated by the difference between the two images with the same amount but opposite defocus $\pm\Delta z$. Since the optimum distance depends on sample properties as well as the detector noise [9, 23, 24], intensity images were taken at 50μm intervals in a range of up to 1.5 mm so that the intensity derivative could be optimized over a range of separations. Note for each sample, recording the entire set of intensities took only about two seconds with our TL-TIE system. The image in the middle (in-focus) plane of the set of images represents the intensity distribution I for which the phase is being sought.

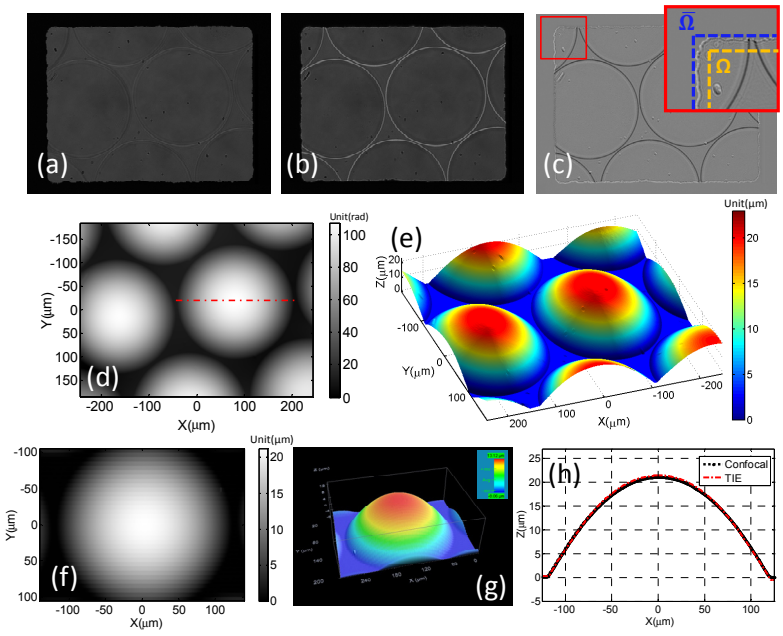

Fig. 5. Characterization of a plano-convex quartz microlens array (pitch 250 μm) (a) In-focus intensity. (b) Defocused intensity distribution ($\Delta z = -550$ μm). (c) Axial intensity derivative, the inset shows the enlarged boxed region. (d) Retrieved phase. (e) Rendered surface plot. (f) Confocal microscopic result. (g) 3-D topography by confocal microscopy. (f) Comparison of the line profiles of single lens.

#210176 - $15.00 USD Received 14 Apr 2014; revised 9 Jun 2014; accepted 26 Jun 2014; published 22 Jul 2014

We firstly verified our method by measuring a 250μm pitch plano-convex quartz microlens array (SUSS MicroOptics, lens diameter 240μm, hex-packed). Figures 5(a) and 5(b) show the in-focus and under-focused ($\Delta z = -550$ μm) intensity distributions. Figure 5(c) shows the estimated axial intensity derivative with the inset showing details of the boxed part. Though the shape of the aperture is not perfect, the boundary signals around the aperture edge can be obviously seen, which corresponds to the second term on the RHS of Eq. (7). The rectangular domain $\bar{\Omega}$ for the solution was defined to encompass the inner aperture region as well as all the boundary signals, as specified by the blue dashed line. The total energy change inside the domain $\bar{\Omega}$ (the LHS of Eq. (8)) was calculated to be negligible (–0.09), verifying the correctness of the energy conservation law and the consistency of experimental data. However, if we narrow down the size of the rectangular domain $\bar{\Omega}$ by 20 pixels to exclude the boundary signals (the reduced domain was denoted as Ω, as specified by the yellow dashed line), the energy change inside the reduced domain Ω increased significantly, from –0.09 to 191.33, indicating there must be some energy exchange through the region boundary. In such case, the TIE phase retrieval problem will become ill-conditioned due to the breakdown of the compatibility condition (Eq. (8)), or equivalently, the missing of appropriate boundary conditions.

With the correctly defined rectangular domain $\bar{\Omega}$ and the DCT-based TIE solver, the phase distribution was retrieved, as shown in Fig. 5(d). Note the TIE phase retrieval is a one-step procedure with the absolute phase directly recovered even the phase excursion is over 100 rads. With a known refractive index of the lens material, the geometrical thickness of the lens can be deduced from the quantitative phase map if the lens has a flat base (e.g., a plano-convex lens):

$$h(x,y) = \frac{OPD(x,y)}{\Delta n} = \frac{\lambda}{n_o - n_m}\frac{\phi(x,y)}{2\pi}, \tag{10}$$

where Δn is the difference between the refractive index of the test object n_o and the medium around the test object n_m. The medium is commonly air, thus n_m is approximated to 1. After the phase-to-thickness conversion, the three dimensional (3-D) height distribution was obtained and shown in Fig. 5(e), revealing that the lens profile has been nicely reconstructed. To validate the quantitative nature of our method, the result was further benchmarked against the white-light scanning confocal microscopy (Sensofar PLμ, 50 × NA = 0.8 objective), as presented in Figs. 5(f) and 5(g). Two line profiles across the center of one individual lens (indicated in Fig. 5(d)) are compared in Fig. 5(e), which demonstrates a good accordance. The maximal height h of the microlens was measured 21.43μm for our method and 21.19μm for confocal microscope. The 1% difference may result from the uncertainties in defocus distance measurements, the imperfection of the rectangular aperture, and the aberration of the imaging system. The temporal phase noise of the system, or the root-mean-square (RMS) repeatability for each pixel, obtained from 2000 times' repeated measurements, is 0.019 rad, which corresponds to a thickness of 4.6 nm for quartz. Given the height profile of the lens, the radius of curvature (ROC) can be calculated by

$$ROC = h/2 + D^2/8h, \tag{11}$$

Where h is the lens height, D is the lens diameter. The calculated ROC is 346.7μm for our method and 350.4μm for the confocal microscopy. Both are in favorable agreement with the manufacturer's specifications (350μm). However, one should note the confocal microscope took about 5 minutes for measuring the single lens profile, resulting from the point-by-point scanning procedure. In contrast, our method is inherently full-field, which is orders of magnitude faster than the confocal microscopy, even allowing for measuring dynamic objects [20].

#210176 - $15.00 USD Received 14 Apr 2014; revised 9 Jun 2014; accepted 26 Jun 2014; published 22 Jul 2014

To demonstrate the advantage of the proposed method and highlights the importance of the boundary signals in the solution of the TIE, we further compare our result to reconstructions from

(1) the standard FFT-based method [12, 13] on the correct domain $\bar{\Omega}$ (with boundary signals),

(2) the proposed DCT-based method on the reduced domain Ω (without boundary signals),

(3) and the standard FFT-based method on the reduced domain Ω (without boundary signals).

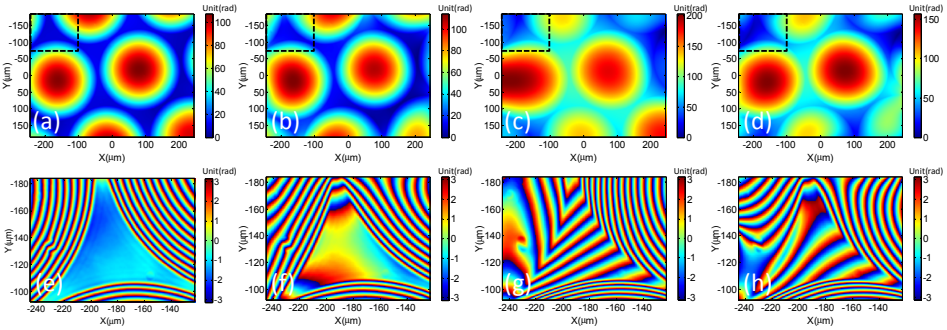

Fig. 6. Comparison of different TIE solutions. The first row shows the recovered phase by (a) our algorithm on the correct domain $\bar{\Omega}$ (with boundary signals), (b) FFT-based algorithm on the correct domain $\bar{\Omega}$, (c) our algorithm on the reduced domain $\bar{\Omega}$ (without boundary signals), (d) FFT-based algorithm on the reduced domain $\bar{\Omega}$. The second row shows the corresponding digitally rewrapped phases of a small portion of from the top-left corner of each result (e)-(f).

When the reconstruction is performed on the reduced domain Ω, the boundary signals are excluded from the input data, and thus the reconstruction algorithms will know nothing about the existence of the aperture. Experimentally, this situation is equivalent to capturing intensity images in the absence of the aperture, and then truncating each image to match the size of Ω. Figure 6 shows the recovered phase distributions from different approaches. To better demonstrate the difference among these methods, the digitally rewrapped phases of a small portion of the top-left corner of each result are magnified, as shown in Figs. 6(e)-6(h), respectively. It should be noted that the Figs. 6(a) and 6(b) are based on the same data set and the same rectangular domain $\bar{\Omega}$ with the boundary signal contained in the axial derivative signal; the only difference is our method is based on DCT while the result shown in Fig. 6(b) uses FFT-based computations. The boundary spoiling effect was clearly seen from the FFT-based solution while can hardly be perceived in our result. The main reason is that the eigenfunctions of the Green's function associated with this Neumann boundary value problem is the Fourier cosine harmonics [25], rather than the general Fourier exponential harmonics, making the DCT-based computations to be the only correct rule. The boundary artifacts can be more severe and lead more significant distortions when the boundary signals are excluded from the input data, or equivalently, without using the aperture, as shown in Figs. 6(c) and 6(d). In such case, neither method could recover the phase distribution correctly due to the ill-posedness of the problem, as we explained previously. These results further confirm that the TIE phase retrieval is essentially a boundary value problem, and the correctness of the solution is justified by both the consistency of the boundary conditions and the use of the appropriate solution.

To accurately quantify the aberrations in optical wavefront related to the shape of the lens profile, the Zernike polynomials expansion was applied to one individual microlens. The results are presented in Fig. 7. We use the first 21 modes, which corresponds to the degree of the Zernike functions from 0 to 7, as illustrated in Fig. 7(b). Figure 7(c) shows the computed coefficients for the microlens data shown in Fig. 7(a). It can be seen that apart from 1st constant offset term (Z_{00}), the 2nd and 3rd tilt term (Z_{01} and Z_{10}), and the 5th defocus term (Z_{20}), the dominant modes in the data is the 13th spherical aberration term (Z_{42}), which is expected from a spherical lens. The Seidel aberrations, such as astigmatism and coma do not

#210176 - $15.00 USD Received 14 Apr 2014; revised 9 Jun 2014; accepted 26 Jun 2014; published 22 Jul 2014

play a significant role. The contributions of higher order (14th - 21st) terms are also negligible. The reconstructed topology data from the computed 21 Zernike coefficients are shown in Fig. 7(d). Qualitatively, the agreement between the original and the reconstructed data is very good. The fitting residual shown in Fig. 7(e), which is the difference between the original and reconstructed data, provides information about the surface roughness of the microlens. The average roughness calculated of the whole lens region is 9.78 nm. But please keep in mind that this transmission result represents an integrated roughness between the upper and lower surfaces of the microlens.

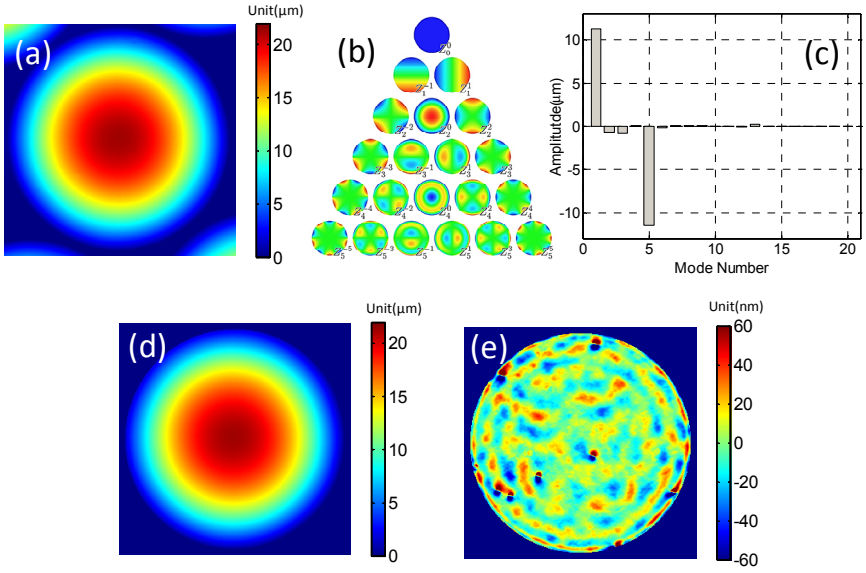

Fig. 7. Aberration and roughness analysis using the Zernike expansion. (a) Raw topography of an individual microlens measured by the TIE. (b) The first 21 Zernike functions used as the basis for the decomposition. (c) Calculated Zernike coefficients. (d) Reconstructed microlens topology using the 21 Zernike coefficients shown in (c). (e) Fitting residual.

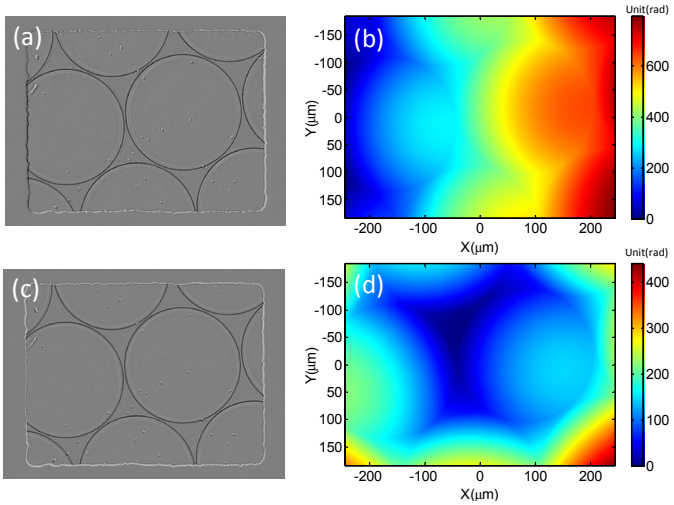

Fig. 8. Measurement results with the misaligned system. (a) and (b) show the axial intensity derivative and the recovered phase when the ETL was slightly shifted horizontally. (c) and (d) show the axial intensity derivative and the recovered phase when the ETL was slightly translated longitudinally.

#210176 - $15.00 USD Received 14 Apr 2014; revised 9 Jun 2014; accepted 26 Jun 2014; published 22 Jul 2014

Finally, it should be noted that though our method is a non-interferometric, single beam method, it is also sensitive to the phase aberration resulting from the optical misalignment. The major aberrations due to optical misalignment are the tilt and defocus. For example, in our current setup, the misalignment between the optical axis and the center of the ETL causes phase tilt, and the misalignment between the Fourier plane of the 4*f* system and the axial position of ETL induces wavefront sphericity. Figure 8 shows the corresponding axial intensity derivatives and the reconstructed phases when we deliberately slightly shift the ETL horizontally or translate it longitudinally. Compared with the well-aligned case (Fig. 5(c)), the most notable change due to the misalignment in the axial intensity derivative is the boundary signals, which can be predicted by Eq. (7). The resultant tilt and phase curvature added to the original phase, as shown in Figs. 8(b) and 8(d). These misalignment-induced aberrations can be compensated with the digital phase mask or double exposure scheme (with sample-free images) that widely-used in digital holographic microscopy [26–28], or more simply rescaling and aligning each intensity images before reconstruction. On the other hand, these abbreviations can be physically eliminated through a rigorous alignment, and a real-time reconstruction software helps a lot in this procedure.

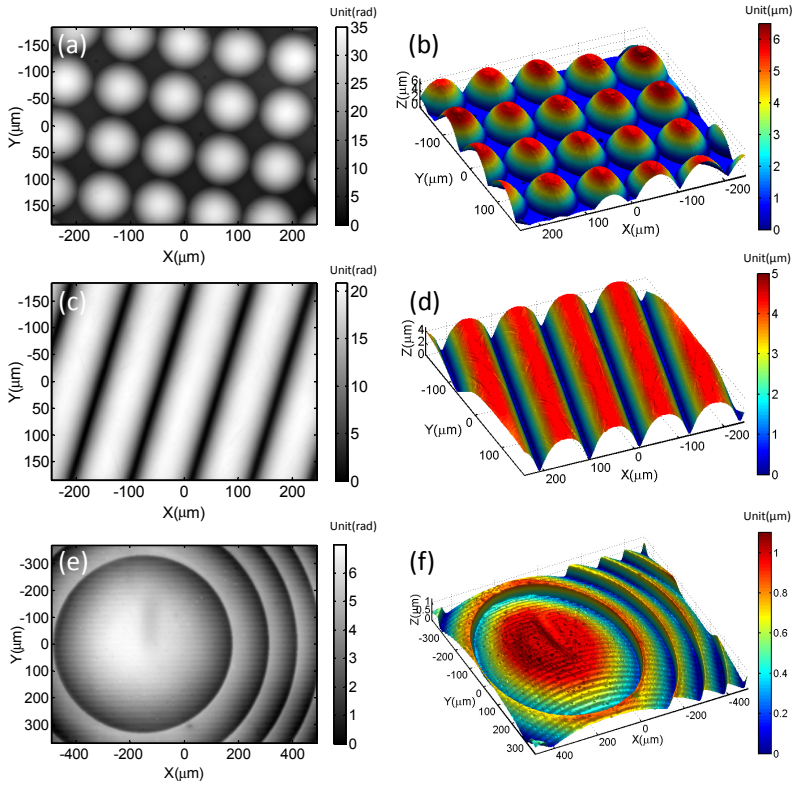

Fig. 9. Measurement results of different types of micro-optics components. First row: a 100μm pitch plano-convex quartz microlens array. Second row: a 100μm diameter cylindrical lens. Third row: a Fresnel lens. The retrieved phase map and the 3-D height distribution are respectively given in the first and second columns.

To demonstrate the versatility of our approach, three other micro-optical components of different shapes were investigated with the same setup. Their corresponding phase distributions and 3-D perspective images are presented in Fig. 9. Figures 9(a) and 9(b) shows the measurement result of another plano-convex quartz microlens array (100 μm pitch, square-packed, measured average maximal height of 5.87 ± 0.12μm). In addition to spherical

#210176 - $15.00 USD Received 14 Apr 2014; revised 9 Jun 2014; accepted 26 Jun 2014; published 22 Jul 2014

microlens, a wide variety of other micro-optical components can be successfully characterized by our system. The measurement results of a quartz refractive cylindrical lens were shown in Figs. 9(c) and 9(d) (lens diameter 100μm, measured average maximal height of 4.35 ± 0.15 μm). Figures 9(e) and 9(f) further provides the measurement results of the central part of a 180mm focal length Fresnel lens. Not only the lens profile was well reconstructed, but the tiny horizontal nicks due to the imperfect fabrication can be clearly seen. These results confirm that our approach is definitely not just limited to spherical lenses, and no modification of the setup or careful adjustment of the sample is required.

5. Discussions

This paper presents the experimental verifications of the recently developed DCT-based TIE solver and illustrates its potential uses in the field of the micro-optics testing. Compared to classical methods, the proposed approach can be considered as an attractive solution as a result of five main features:

- It is non-interferometric, works with partially coherent illuminations. The whole system is simple, low cost, light weight, and fully compatible with ordinary microscopes.
- It is a single-beam method and thus inherently much less sensitive to external perturbations (vibration) compared to interferometry.
- It directly gives an unwrapped phase without the need for phase unwrapping.
- Its accuracy is close to much more complex, time-consuming and expensive methods but its speed much faster since there is no moving part in the whole system. The measurement accuracy is thus not intrinsically limited by the precision of the control of moving parts, such as piezoelectric transducers and motorized sample stages.
- It is simple to use without adaptations to investigate a wide variety of micro-optical component shapes.

On the other hand, some important issues must be taken in into considerations in the practice of our approach:

Firstly, since the TIE implies the phase is a continuous function, our method cannot be applied to reconstruct the phase distribution with discontinuities. Though no need for unwrapping is an advantageous feature of the TIE, the famous "2π ambiguity problem" is not fundamentally solved for the same reason [29].

Secondly, as the axial intensity derivative is calculated via finite differences from two defocused intensities, the accuracy of phase reconstruction relies heavily on the separation between the measurement planes [23, 30]. The phase errors originate from the noise in the captured intensities and the nonlinear error component related to the finite difference approximation. Since the low-frequency phase structure shows less phase contrast than the high-frequency phase structure as the wave propagation [21, 31, 32], the TIE is very sensitive to low-frequency artifacts, especially when the defocus distance is chosen too small. Using a larger separation provides a better signal to noise ratio; nevertheless, the breakdown of the linear approximation that underlies the finite difference approximation induces nonlinear errors that will reduce the phase resolution. To obtain a compromise between nonlinearity error and the low-frequency noise, there exists an optimal distance which is dependent on both the maximum physically significant frequency of the object and the level of noise [9, 23, 24]. In this work, the intensity images were taken at equal intervals over a large z range (1.5 mm), then a program was used to have a quick estimation of the noise profile in order to find the best possible distance for each sample before reconstruction. It should be noted that more sophisticated approaches using higher-order finite difference [9, 24] can also be used to minimize nonlinearity error and noise effect at the cost of higher computational complexity.

Thirdly, to generate the required boundary values for the proposed approach, the object field must be confined with a hard-edged aperture. However, for microscopic applications, it is quite hard to fabricate small apertures and properly align it for different test objects in practice. In this work, we choose to place the aperture in the intermediate plane rather than the

#210176 - $15.00 USD Received 14 Apr 2014; revised 9 Jun 2014; accepted 26 Jun 2014; published 22 Jul 2014

real object plane of the microscope to overcome these difficulties. However, in this case the through focus intensity stack can no longer be captured via simply adjusting the sample stage. Instead, an additional image relay system (4*f* system combined with a tunable lens in our case) is required to defocus the "image" of the object (where the aperture is located).

Fourthly, our method requires precise alignment of all the involved optical elements. As shown in Fig. 8, the optical misalignment can easily create erroneous axial intensity signal at the aperture boundary line so that the whole phase reconstruction will be spoiled by the aberration. This phenomenon is rarely observed throughout the TIE literature - almost all the phases reconstructed by TIE are perfectly "flat", free from such kind of aberrations without any explicit aberration compensation procedure. However, does this mean all the results are obtained based on very nice optical configurations that are free from such kind of aberrations? The answer of course is ***NO***! The truth is the TIE is ***blind*** to such kind of aberration if the boundary signals cannot be acquired [15, 33, 34]. Though these aberrations are not what we want, as a *quantitative* phase retrieval method, it is favorable for our approach to be able to reliably reconstruct all kinds of phase distributions regardless of whether they are real signals or the optical aberrations.

Finally, it should be noted that the validity of the TIE relies on the paraxial approximation [5, 31, 35], while the microscope is a non-paraxial system. But what we actually measure is not the phase of the object but the phase of the image corresponding to the magnified object in the image plane. Since the NA in the image plane is greatly reduced compared to the real object NA ($NA_{\text{image}} \approx NA_{\text{obj}}/M$, where M is the magnification of the optical system), the paraxiality can be regarded as a reasonable assumption [32].

6. Conclusions

In this paper, we have demonstrated that the TIE-based phase retrieval approach presented here allows for optical inspection of micro-optical components. It is implemented based on a conventional bright-field microscope and use the partially coherent illumination. Thus it possesses better spatial resolution and less suffers from the speckle noise than interferometry. Furthermore, with regard to the state of the art in phase-retrieval by means of the TIE, the technique has another two major advantages: First, it completely erases the boundary artifacts by simply introducing an aperture in the intermediate image plane, without requiring any assumptions or *a prior* knowledge about the test object and the setup. Second, in contrast to existing approaches, with use of an ETL, the measurement time is considerably reduced and no further mechanical adjustment is needed during the measurement. The validity and practicality of the proposed method have been demonstrated with a wide variety of micro-optical components, suggesting that it is a simple, fast, and accurate measurement technique for the micro-optics inspection.

Acknowledgments

The authors would like to thank Yang Yu from Ngee Ann Polytechnic for fabricating the aperture. This project was supported by the Research Fund for the Doctoral Program of Ministry of Education of China (No. 20123219110016), and the National Natural Science Foundation of China (No. 61271332). Chao Zuo gratefully acknowledges the financial support from China Scholarship Council (No. 201206840009).

#210176 - $15.00 USD Received 14 Apr 2014; revised 9 Jun 2014; accepted 26 Jun 2014; published 22 Jul 2014